Solar radiative forcing of aerosol particles near the Taklimakan desert during the Dust Aerosol Observation-Kashi campaign in Spring 2019

Li Li[1], Zhengqiang Li[1], Wenyuan Chang[2], Yang Ou[1], Philippe Goloub[3], Chengzhe Li[4], Kaitao Li[1], Qiaoyun Hu[3], Jianping Wang[1], Manfred Wendisch[5]

[1]Aerospace Information Research Institute, Chinese Academy of Sciences, Beijing 100101, China
[2] Institute of Atmospheric Physics, Chinese Academy of Sciences, Beijing 100029, China
[3] Laboratoire d'Optique Atmosphérique, Université de Lille 1/CNRS, Lille 59655, France
[4] Department of Chemical and Biochemical Engineering, University of Iowa, Iowa 52242, USA
[5] Leipzig Institute for Meteorology, Leipzig University, Leipzig 04103, Germany

Correspondence to: Zhengqiang Li (lizq@radi.ac.cn)

Abstract. The Taklimakan desert is a main and continuous source of Asian dust particles causing a significant direct aerosol solar radiative forcing (*ASRF*). In order to improve the accuracy of the estimation of dust radiative forcing effects, the Dust Aerosol Observation-Kashi (DAO-K) campaign was carried out near the Taklimakan desert in April 2019. The objective of the campaign is to provide comprehensive parameters such as: dust optical and microphysical properties, vertical distribution and surface albedo, for the calculation of *ASRF*. The measurements were employed in radiative transfer (RT) simulations and the estimations are improved by considering the actual measured atmospheric profiles and diurnal variations of land surface albedo in addition to reliable aerosol parameters. The RT model estimates the *ASRF* results in average daily mean cooling effects of -19 W m^{-2} at the top of atmosphere and -36 W m^{-2} at the bottom of atmosphere during the DAO-K campaign. The Weather Research and Forecasting model with Chemistry (WRF-Chem) with assimilations of the aerosol optical depth and PM$_{2.5}$ and PM$_{10}$ concentrations measurements is prone to overestimate the radiative forcing effects of dust aerosols. The percent difference of daily mean *ASRF* between the two simulations are greater than 50% in heavy dust episode. Ground-based observations of downward irradiances have validated that the RT simulations are in good agreement with simultaneous observations, whereas the WRF-Chem estimations exhibit obvious discrepancy with these independent measurements. Data assimilations can partly reduce the discrepancy, but there is still room for improving the WRF-Chem simulation of dust aerosol radiative forcing.

1 Introduction

Atmospheric aerosol particles play a vital role in regional and global climate changes, directly by modifying the radiation balance of the Earth-atmosphere system, and indirectly by altering cloud radiative properties, as well as cloud development and precipitation through acting as cloud condensation nuclei and/or ice nuclei (Twomey, 1977; IPCC, 2007; Lenoble et al.,

2013; Werner et al., 2014). Mineral dust is the most abundant aerosol type in the atmosphere (Ansmann et al., 2011), which has a tremendous impact on radiation budget, not only through scattering process, but also due to absorption of solar (0.3~5 μm), also called shortwave (SW) radiation (Otto et al., 2007; García et al., 2012; Valenzuela et al., 2012; Lenoble et al., 2013), with potential dynamic consequences (Wendisch et al., 2008). The dust radiative effects also depend on the surface albedo

35   over the desert (Bierwirth et al., 2009). As one of the largest sandy deserts in the world, the Taklimakan Desert (TD) located in the Xinjiang Uyghur Autonomous Region of China (Fig. 1) is a main source region of Asian dust, which influences many areas in Eastern Asia, the Tibetan Plateau, the Pacific Ocean, even North America and Greenland (Bory et al., 2003; Mikami et al., 2006; Huang et al., 2009; Chen et al., 2013). Thus, an assessment of the Taklimakan aerosol solar radiative forcing (*ASRF*, defined as the difference of the net solar irradiance with and without aerosols presence) is important to evaluate regional

40   and global climate changes. However, it is a challenging due to the high aerosol loading and complex light scattering properties of mineral dust, as well as high surface albedo over desert.

Numerous efforts have investigated the radiative effects of mineral dust over the Taklimakan region using radiative transfer (RT) model, or the regional and global meteorological and climate model (Huang et al., 2009, 2014; Sun et al., 2012; Chen et al., 2013, 2014, 2018). Huang et al. (2009) employed the Fu-Liou RT model to simulate the Taklimakan *ASRF* during

45   the dust episodes in the summer of 2006, and reported that the TD dust aerosols have a significant impact on solar radiation with the average daily mean radiative effects of 14 W m^{-2} at the top of atmosphere (TOA), 79 W m^{-2} in the atmosphere, and -65 W m^{-2} at the bottom of atmosphere (BOA). Sun et al. (2012) also reported negative *ASRF* of dust particles at BOA with the strongest values in spring, reaching up to -25 W m^{-2} in the three main desert regions of TD, western Inner Mongolia, and northern Xinjiang. For these estimates, simulations by the regional climate model version 4 (RegCM4) for the years of

50   2000~2009 were used. Chen et al. (2014) applied the Weather Research and Forecasting model with Chemistry (WRF-Chem) to investigate the seasonal and inter-annual variations of dust radiative forcing over TD during 2007~2011, and reported that the dust radiative forcing have relatively small inter-annual variation but a distinct seasonal course with maximum values in late spring and early summer. According to WRF-Chem simulations, the total (SW plus longwave) TD dust direct radiative forcing results in a TOA cooling of -5 W m^{-2}, atmospheric warming of up to 9 W m^{-2}, and BOA cooling of up to -14 W m^{-2}

55   (Chen et al., 2014). Li et al. (2018) adopted the Santa Barbara (discrete ordinate radiative transfer) DISORT Atmospheric Radiative Transfer (SBDART) simulations to present the multi-year average SW aerosol radiative forcing of -16 W m^{-2} at TOA and -18 W m^{-2} at BOA at the edge of TD, Kashi station.

Large uncertainties in simulations of radiative forcing could cause significant errors in estimating the modulate effects of mineral dust aerosols on the climate (Huang et al., 2009). From previous researches, performances of models in simulating of

60   dust *ASRF* have been indirectly validated by comparing with the observations of aerosol optical depth (*AOD*), aerosol extinction profile, aerosol single scattering albedo (*SSA*), and particle size distribution (Zhao et al., 2010; Chen et al., 2014). Nevertheless, comparison of *ASRF* or irradiance is indispensable to provide direct evidence for evaluating the models. In this paper, we concentrate on estimation of direct solar radiative forcing of dust-dominated aerosols by the SBDART radiative transfer model with appropriate satellite and ground-based observations as inputs. The *ASRF* simulations will be

65 comprehensively evaluated by comparison with the results of WRF-Chem simulations, ground-based irradiance measurements, as well as the AErosol RObotic NETwork (AERONET, http://aeronet.gsfc.nasa.gov) operational products (Holben et al., 1998).

The paper begins with a brief introduction of the Dust Aerosol Observation-Kashi (DAO-K) field campaign, and an introduction of the multi-source observations and data in Sect. 2. Methods to estimate *ASRF* by improving the input parameters in RT simulation and by employing data assimilations in the WRF-Chem simulation are described in Sect. 3. Sect. 4 presents

70 the instantaneous and daily mean results of *ASRF* simulated by RT model during the DAO-K field campaign. The influences of the atmosphere and surface conditions on the results are discussed. They are also evaluated by comparing with AERONET operational products, WRF-Chem simulations, and simultaneous irradiance measurements. Summary and conclusions are given in Sect. 5.

2 Dust Aerosol Observation-Kashi field campaign

75 ### 2.1 Experimental site and instrumentation

The Dust Aerosol Observation-Kashi (DAO-K) field campaign with comprehensive observations of physical, chemical, and optical properties of aerosol particles, radiative properties, vertical structures of atmosphere, and land surface albedo in this region was designed to provide high quality data for aerosol radiative forcing estimates. Kashi is located in the vicinity of the Taklimakan Desert; it is surrounded by the Tianshan Mountains in the north, the Pamir Plateau in the west, and the Kunlun

80 Mountains in the south (Fig. 1). Kashi represents a typical place affected by dust aerosols, local anthropogenic pollution, and pollution transported from surrounding arid and desert areas. The DAO-K field campaign was conducted at the Kashi campus of the Aerospace Information Research Institute, Chinese Academy of Sciences (39.5˚N, 75.9˚E, 1320 m above mean sea level). The campus hosts a long-term observation station within the Sun-sky radiometer Observation NETwork (SONET, www.sonet.ac.cn) (Li et al., 2018). According to the SONET measurements during more than six years, the Kashi site is

85 frequently affected by dust particles, where the multi-year average *AOD* is up to 0.56±0.18 at 500 nm, moreover, the Ångström exponent (*AE*, 440~870 nm) and fine-mode fraction (*FMF*) at Kashi are the lowest among all sites in China. Every year, *FMF* reaches the lowest value, and the volume particle size distribution presents a pre-dominant coarse mode from March to May, due to the frequent dust invasions in spring (Li et al., 2018). The DAO-K intensive field campaign was carried out in April 2019 and lasted for nearly a month. During the campaign, several dust processes were observed by coordinated deployment of

90 multiple in-situ and remote sensing platforms and instruments based on passive and active detection technologies.
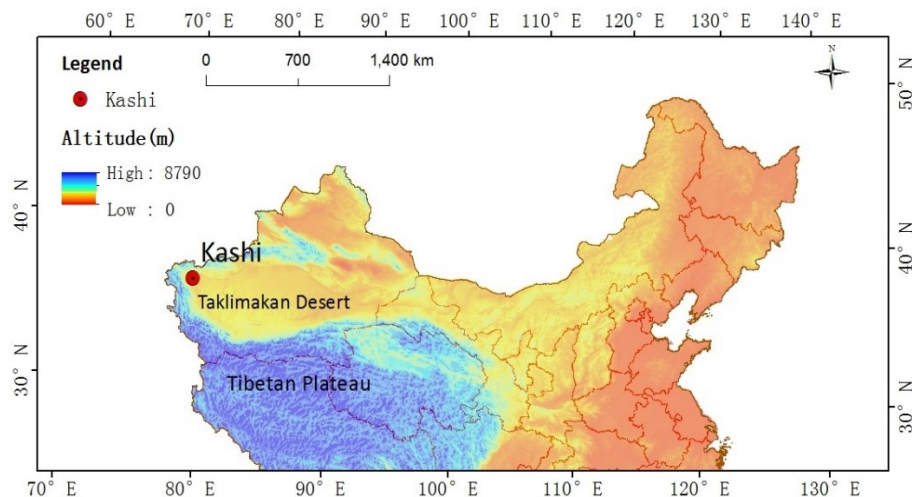
Figure 1: The location of the observation site (Kashi) during the DAO-K field campaign.

Fig. 2 shows the setup of the ground-based instrumentation in the DAO-K campaign, and Tab. 1 lists the corresponding ground-based and satellite retrieved parameters applied in *ASRF* estimation and evaluation in this study. Four sun-sky radiometers, including a polarized sun-sky-moon radiometer CE318-TP (#1150), two unpolarized sun-sky-moon radiometers CE318-T (#1098 and #1141), and a polarized sun-sky radiometer CE318-DP (#0971), were deployed to derive the volume aerosol properties of *AOD*, *AE*, *SSA*, and asymmetry factor (i.e., *g*) for model inputs (Li et al., 2014, 2015). All the radiometers have been calibrated rigorously before the field campaign. CE318 #1150 and #1141were calibrated at AERONET Izaña Observatory by Langley plot approach with the accuracy of *AOD* about 0.25%~0.5% at the visible and near-infrared bands and calibrated by integrating sphere with the uncertainty of radiance about 3%~5% (Holben et al. 1998; Li et al., 2018). *AOD*-related measurements and radiance measurements of CE318 #1098 and #0971 were calibrated via inter-comparison with a master instrument using Langley method and using a vicarious/transfer calibration method, respectively (Li et al., 2008; 2018). The intensive measurements of four radiometers in this campaign aim to verify the consistencies of calibration coefficients. The volume aerosol parameters were combined with four radiometer measurements following SONET level 1.5 data criteria (Li et al., 2018). Observations from the CE318-T #1141 during the DAO-K campaign also joined in the AERONET dataset. The consistency of the products following the AERONET and SONET retrieval frameworks has been validated by Li et al. (2018). In the retrieval frameworks, the dust particles were considered as non-spherical particles, which were modelled by randomly oriented spheroids (Dubovik et al., 2006).

A solar radiation monitoring station, consisting of an EKO MS-57 pyrheliometer and two MS-80 pyranometers, was used for measuring the direct, diffuse and total solar irradiances in the range of 0.28~3.0 μm. The pyrheliometer and pyranometers have been calibrated before the campaign with uncertainties of 0.55 % and 0.66 %, respectively. They satisfy the requirements of class A under the ISO 9060:2018 with fast response time <0.2 s and <0.4 s, separately, which make them have excellent performances in understanding of the dynamics of solar irradiances in the atmosphere. Multiwavelength Mie-Raman

polarization lidar (LILAS) developed by the Laboratoire d'Optique Atmosphérique (LOA) of University of Lille, was equipped
115   with three elastic wavelengths (all linearly polarized) at 355, 532, 1064 nm and three Raman wavelengths at 387, 530, 408 nm,
from which the vertical distribution of multiple optical and physical properties of dust aerosols (Veselovskii et al., 2016, 2018;
Hu et al., 2019) can be obtained. The backscattering coefficient profile at 355 nm wavelength was applied in this study to
distinguish the two-layer structure of dust. $PM_{2.5}$ mass concentration was measured by a continuous particulate monitor. The
hourly PM_{10} mass concentrations in Kashi were collected from the routine measurements operated by China National
120   Environmental Monitoring Center (CNEMC). The cloud-cover automatic observation instrument equipped with two wide-
dynamic full-sky visible and infrared imagers, detected cloud amount and distribution in the sky during day and night with 10
min (or less than 10 min) resolution. Atmospheric profiles during the campaign were collected from sounding balloon
measurements operated by Kashi regional meteorological bureau.

In addition to the ground-based observations, the satellite products of Moderate resolution imaging spectroradiometer
125   (MODIS)/Terra+Aqua were adopted to derive the diurnal-change of the surface albedo (Schaaf and Wang, 2015). Ozone
profiles obtained by the Ozone Monitoring Instrument (OMI)/Aura (Bhartia et al., 1996) were applied in the RT model input.
Considering different durations of various measurements, in this study we calculated and discussed the *ASRF* from 2 to 25
April 2019, when simultaneous measurements are available.
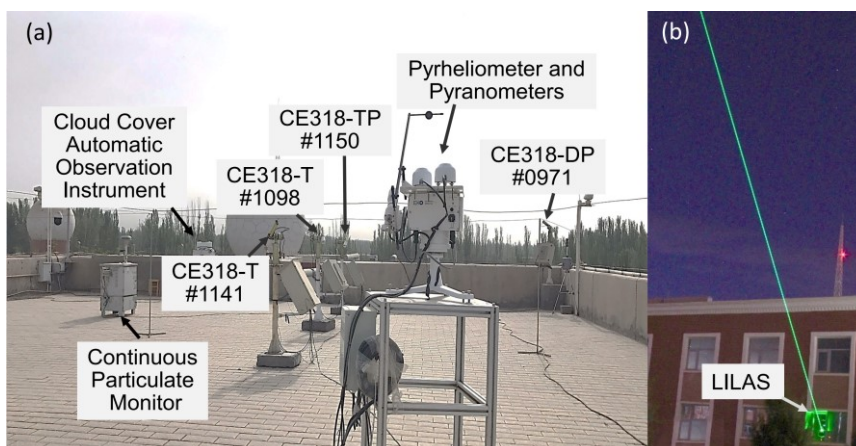
130   **Figure 2: Setup of experimental apparatus of the DAO-K field campaign (a) on the roof, (b) in door.**

Table 1: Parameters used in this study from experimental and routine measurements during the DAO-K campaign.

Instrument	Parameter	Duration
Cimel sun-sky radiometer	aerosol optical depth (*AOD*)	1/4/2019 – 25/4/2019
	Ångström exponent (*AE*)	
	single scattering albedo (*SSA*)	
	asymmetry factor (*g*)	

EKO MS-57 Pyrheliometer and MS-80 Pyranometers	direct-normal solar irradiance (W m^{-2}) diffuse solar irradiance (W m^{-2}) total solar irradiance (W m^{-2})	2/4/2019 – 28/4/2019
Multiwavelength Mie-Raman polarization lidar (LILAS)	backscattering coefficient (km^{-1} sr^{-1})	4/4/2019 – 28/4/2019
ASC200 Cloud Cover Automatic Observation Instrument	full-sky visible image	2/4/2019 – 27/4/2019
METONE BAM-1020 Continuous Particulate Monitor	$PM_{2.5}$ mass concentration (mg m^{-3})	1/4/2019 – 28/4/2019
Ambient air quality continuous automated monitoring system	PM_{10} mass concentration (mg m^{-3})	1/4/2019 – 30/4/2019
Moderate resolution imaging spectroradiometer (MODIS)/Terra+Aqua	shortwave bidirectional reflectance distribution function (BRDF) parameters shortwave black-sky albedo shortwave white-sky albedo	1/4/2019 – 30/4/2019
Sounding balloon	Vertical distributions of the atmospheric pressure, temperature, and relative humidity	1/4/2019 – 30/4/2019
Ozone Monitoring Instrument (OMI)/Aura	Ozone (O$_3$) profile	1/4/2019 – 30/4/2019

2.2 Aerosol properties during the DAO-K campaign

Fig. 3 illustrates the time series of *AOD*, *AE*, and corresponding $PM_{2.5}$ and PM_{10} mass concentrations measured during the DAO-K campaign. The average value of *AOD* at 550 nm is 0.65 during the campaign. According to *AOD*, five high aerosol

135 loading episodes are identified: UTC 9:26~12:15 on 2/4/2019, 9:13 on 3/4/2019 until 5:11 on 5/4/2019, 1:52 on 8/4/2019 until 4:20 on 10/4/2019, 1:47 on 13/4/2019 until 12:32 on 16/4/2019, 1:30 on 24/4/2019 until 4:11 on 25/4/2019. The highest values of *AOD* at 550 nm (2.3) were observed from 24/4/2019 to 25/4/2019 during a severe dust storm event. From Fig. 3, there is an obvious negative correlation between *AOD* and *AE*. For these high aerosol loading episodes, the *AE*s show very low values, suggesting that the heavy aerosol outbreaks at Kashi were dominated by dust particles. As a qualitative indicator of aerosol

140 particle size, the values of *AE* are always less than 1.0 during the DAO-K campaign, suggesting that aerosol particles around the Taklimakan desert are mainly dominated by coarse particles (even for clear situations). This is consistent with the results

obtained in a previous study (Fig. 4 in Li et al., 2018). Comparatively high values of *AE* (>0.4) can be observed on 7, 12, 19, and 23 April 2019, implying enhanced local anthropogenic pollution and relatively small particle enrichments for these days.

145   The average values of *PM*~2.5~ and *PM*~10~ mass concentrations corresponding to measuring times of CE318 are 0.08 and 0.25 mg m^-3 during the campaign, respectively. The time series of *PM*~2.5~ and *PM*~10~ mass concentrations generally concur with that of *AOD*. However, for some days such as 19 and 23 April 2019, relatively high *PM*~2.5~ corresponding to low *AOD* has been observed, also indicating the enhanced influences of anthropogenic pollutions in these cases. But for 7 and 12 April 2019, high *AE* values corresponding to low *PM*~2.5~ values could be down to the very low turbidity conditions. The errors in computations of *AE* significantly increase under low aerosol loading conditions (Kaskaoutis et al., 2007). The maximum *PM*~10~ concentration

150   during the heavy dust storm episode from 24 to 25 April 2019 was up to 4 mg m^-3. However, only moderate values of *PM*~10~ are shown in Fig. 3 because there was no CE318 measurement around the peak time of dust outbreak.
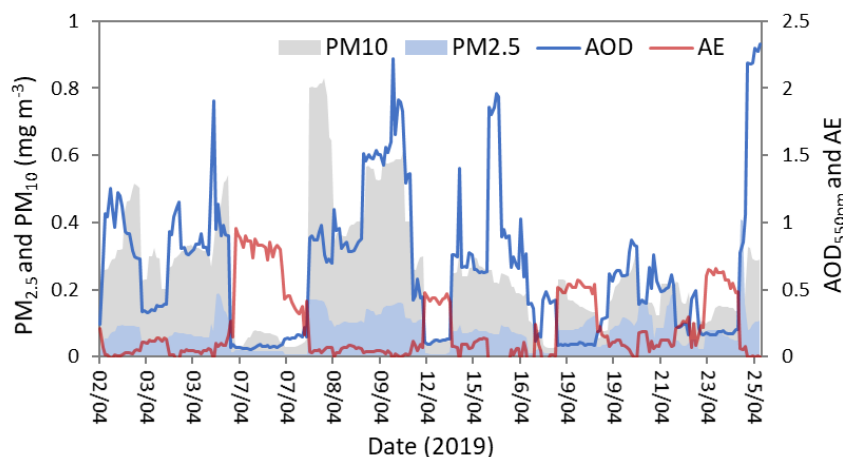
Figure 3: Variations of aerosol optical depth (550 nm), Ångström exponent (440~870 nm), *PM*~2.5~ and *PM*~10~ mass concentrations at Kashi site during the DAO-K campaign.

155   **3 Estimation of aerosol solar radiative forcing**

3.1 Definition of aerosol solar radiative forcing

The direct solar radiative forcing of atmospheric aerosols can be calculated as (Babu et al.,2002; Adesina et al., 2014; Esteve et al., 2014)

$$ASRF_{\mathrm{TOA}} = F_{\mathrm{TOA}}^{\mathrm{a}} - F_{\mathrm{TOA}}^{0} , \qquad (1)$$

160   $$ASRF_{\mathrm{BOA}} = F_{\mathrm{BOA}}^{\mathrm{a}} - F_{\mathrm{BOA}}^{0} , \qquad (2)$$

$$ASRF_{\mathrm{ATM}} = ASRF_{\mathrm{TOA}} - ASRF_{\mathrm{BOA}} , \qquad (3)$$

$$F = F^{\downarrow} - F^{\uparrow}, \tag{4}$$

where $ASRF_{TOA}$, $ASRF_{BOA}$ and $ASRF_{ATM}$ denote the direct aerosol solar radiative forcing at the TOA, BOA and in ATM, respectively. F^a and F^0 indicate the net irradiances with and without aerosols, respectively. $F^{\downarrow}$ and $F^{\uparrow}$ separately represent the downward and upward irradiances. All the above quantities are in W m^{-2}. The radiative forcing efficiency is defined as the rate at which the atmosphere is forced per unit of aerosol optical depth at 550 nm (García et al., 2008, 2012):

$$ASRFE = ASRF \Big/ \tau_{550}, \tag{5}$$

where $ASRFE$ (in W m^{-2} τ_{550}^{-1}) is the aerosol solar radiative forcing efficiency at the TOA, BOA, or in ATM. Since the effects of aerosol loading on radiative forcing have been eliminated, radiative forcing efficiency has unique advantage on evaluation of the direct radiative effects of different types of aerosols (García et al., 2008).

3.2 Radiative transfer model simulation

The focus of this study is to quantify of direct $ASRF$ and $ASRFE$ at the TOA, BOA, and in ATM under cloud-free sky conditions by the SBDART radiative transfer model with reliable satellite and ground-based observations during the DAO-K campaign as model inputs. SBDART is a radiative transfer software tool that has been widely adopted in atmospheric radiative energy balance studies (Ricchiazzi et al.,1998; Li et al., 2018). The discrete ordinate method is adopted in the code, which provides a numerically stable algorithm to solve the equations of plane-parallel radiative transfer in a vertically inhomogeneous atmosphere (Ricchiazzi et al.,1998). The simulations cover the same wavelength range (i.e., 0.28~3.0 μm) with the pyranometer for the convenience of comparison. Simulations of the $ASRF$ by RT model are susceptible to the input conditions including the aerosol properties, atmosphere profile (including ozone), and land surface albedo. They were specified based on the high-quality dataset obtained in the DAO-K campaign.

3.2.1 Setting of aerosol properties

The aerosol properties including AOD, SSA, AE, and g retrieved from the radiometer observations at four bands with the central wavelengths at 440, 675, 870, and 1020 nm. They were applied in the instantaneous radiative forcing and efficiency calculations at the corresponding observing time. The aerosol properties in the SW range are obtained by interpolation and extrapolation using parameters in the above mentioned four bands. For daily mean $ASRF$ simulation, the averaged aerosol parameters (i.e., AOD, SSA, AE, and g) obtained from the day-time radiometer observations were used as alternatives of the daily mean aerosol properties. The daily mean aerosol radiative forcing and efficiency were calculated by taking the average of the 24 instantaneous values on an hourly basis.

3.2.2 Setting of atmospheric profile

190   In addition to aerosol properties, atmospheric profiles of thermodynamic properties are important for *ASRF* calculation. The vertical distributions of air pressure, temperature, water vapor, and ozone densities have obvious influences on the direct and diffuse solar irradiances at the BOA. The predefined atmospheric profiles in RT model (e.g., tropical, mid-latitude summer, mid-latitude winter, sub-arctic summer, sub-arctic profiles) are different from Kashi local conditions. Within the *ASRF* simulations, the predefined profiles have been replaced by the actual measurements conducted during the campaign. Vertical

195   distributions of the atmospheric pressure, temperature, relative humidity can be obtained by atmospheric sounding twice a day around 0:00 and 12:00 UTC at Kashi. The profiles of ozone density (in g m^{-3}) was deduced from the OMI/Aura OMO3PR product (in DU) (Bhartia et al., 1996). Two atmospheric profiles were specified for each day. The profile closest to the simulated moment of *ASRF* was adopted for both of instantaneous and daily mean aerosol radiative forcing estimates.

3.2.3 Setting of land surface albedo

200   Land surface albedo (LSA) is another key factor to influence the radiation budget, mainly due to its significant impact on the SW upward irradiance (Liang, 2004; Bierwirth et al., 2009; Tegen et al., 2009; Jäkel et al., 2013; Stapf et al., 2019). Shortwave land surface albedo α_{SW}, also known as blue-sky albedo, can be calculated from the black-sky albedo (BSA) $\alpha_{\mathrm{SW}}^{\mathrm{BSA}}$ and white-sky albedo (WSA) $\alpha_{\mathrm{SW}}^{\mathrm{WSA}}$ weighted by the fraction of diffuse skylight radiation (Schaaf et al., 2002; Wang et al., 2015):

$$\alpha_{\mathrm{SW}}(\theta_{\mathrm{s}}, \varphi_{\mathrm{s}}) = f_{\mathrm{diffuse,SW}} \, \alpha_{\mathrm{SW}}^{\mathrm{WSA}} + (1 - f_{\mathrm{diffuse,SW}}) \, \alpha_{\mathrm{SW}}^{\mathrm{BSA}}(\theta_{\mathrm{s}}, \varphi_{\mathrm{s}}), \tag{6}$$

205   where $f_{\mathrm{diffuse,SW}}$ denotes the fraction of diffuse radiation in the solar spectral range. $(\theta_{\mathrm{s}}, \varphi_{\mathrm{s}})$ specifies the incident solar geometry (i.e., solar zenith angle and solar azimuthal angle).

     The shortwave WSA and BSA are provided by the MODIS BRDF/Albedo Science Data Product MCD43A3, which is produced daily using 16 days of MODIS/Terra+Aqua data. MCD43A3 only delivers the surface albedo products at local solar noon. However, diurnal variations of LSA cannot be ignored, which has been demonstrated by several previous studies (Lewis

210   and Barnsley, 1994; Lucht et al., 2000; Wang et al., 2015). There will be an obvious bias in estimating daily solar radiation when simply using the local noon value as a surrogate of daily mean albedo (Wang et al., 2015). As for the weighting parameters of the RossThickLiSparseReciprocal BRDF model (i.e., isotropic, volumetric, and geometric), the changes within 16 days are subtle. Therefore, the daily three model weighting parameters over the SW band afforded by MCD43A1 are adopted to derived the WSA and BSA (the latter is as a function of incident solar direction) at different simulated moments of

215   *ASRF*. The fraction of diffuse radiation can be calculated by the ratio of diffuse solar irradiance to total solar irradiance, which mainly depends on the solar zenith angle, aerosol and cloud conditions. The diffuse and total irradiances measured by pyranometers with 1 min resolution are applied in this study to calculate the fraction of diffuse radiation.

Fig. 4 gives diurnal variations of LSA and corresponding full-sky visible images under four typical sky conditions at Kashi. For the clear-sky conditions (almost the whole day of 7/4/2019 and afternoon of 12/4/2019), LSA changes distinctly

220 for different time. High values of LSA can be observed in the early morning and the late afternoon. Meanwhile, the extreme value of LSA in the morning (0.253) is greater than that in the afternoon (0.218), which has been supported by some other field observations (Minnis et al., 1997; Wang et al., 2015). The local noon albedo shows very low value. The daily mean albedo under the clear-sky condition (0.199) is appreciably greater than the local noon albedo (0.173). However, in the dust-polluted (almost the whole days of 9/4/2019 and 25/4/2019) and cloudy (the morning of 12/4/2019) sky conditions, the changes

225 of LSA are not as severely as in the clear-sky conditions. Nevertheless, the local noon albedo still cannot reflect the effects of aerosol and cloud variations on land surface albedo. Thus, diurnal-changed LSA and the daily mean albedo were adopted in the instantaneous and daily mean *ASRF* simulations, respectively. It is predictable that estimations of instantaneous and daily mean aerosol radiative forcing can be improved by considering diurnal variations of LSA instead of local noon albedo.
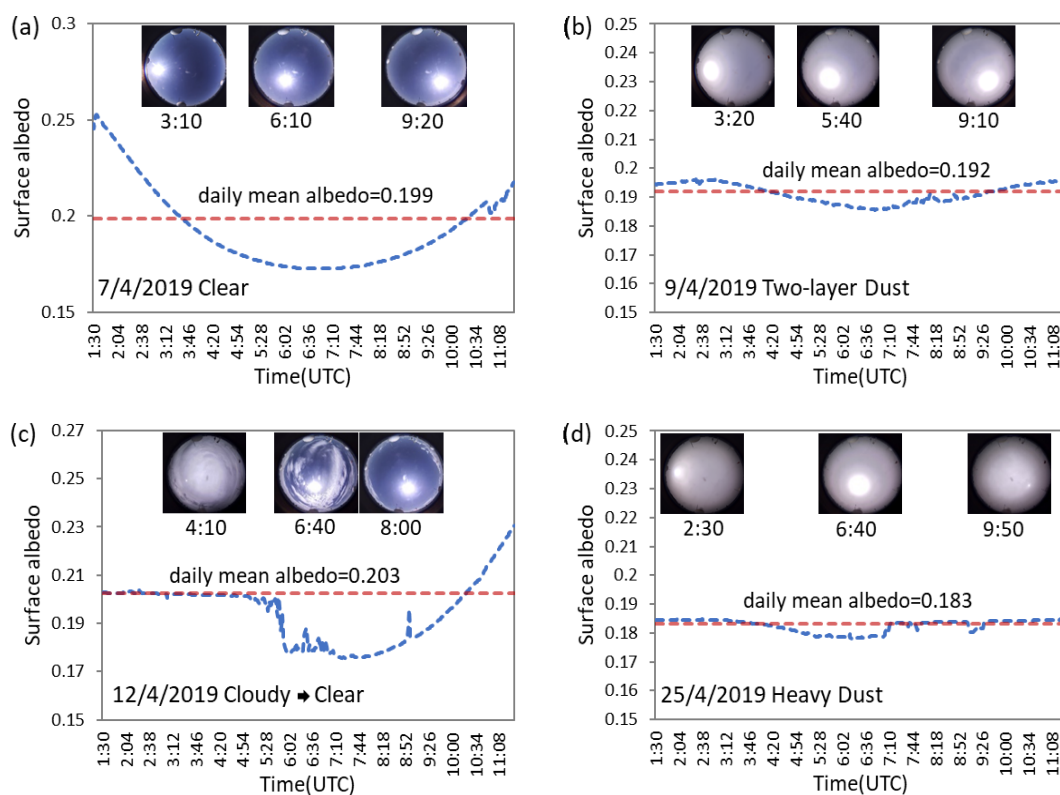
Figure 4: Diurnal variations of blue-sky albedo and corresponding full-sky visible images under different sky conditions at Kashi
230 **(a) clear case, (b) two-layer dust case, (c) clouds early/clearing late case, (d) heavy dust case.**

3.3 WRF-Chem model simulation

3.3.1 Forecast model

The Weather Research and Forecasting model with chemistry (WRF-Chem) model version 4.0 (Grell et al., 2005; Fast et al., 2006) was also used to simulate the *ASRF* at Kashi. The simulations were configured in a 9 km domain centered at Kashi site
235   with 45×45 grid points and 41 vertical levels that extended from the surface to 50 hPa. The main physical options used for this study included the Purdue Lin microphysics scheme, the unified Noah land surface model, the Yonsei University (YSU) scheme for planetary boundary layer meteorological conditions, and the Rapid Radiative Transfer Model for General Circulation Models (RRTMG) for SW and longwave radiation. The Carbon Bond Mechanism (CBMZ) was used for the Gas-phase chemistry processes (Zaveri and Peters, 1999), which includes aqueous-phase chemistry. The aerosol chemistry was
240   based on the Model for Simulating Aerosol Interactions and Chemistry (MOSAIC; Zaveri et al., 2008) with four size bins (0.039~0.156 μm, 0.156~0.625 μm, 0.625~2.5 μm, 5.0~10.0 μm dry diameters). The sum of aerosol mass concentrations in the first three size bins constructs the concentration of $PM_{2.5}$ and the sum of the four size bins gives the concentration of PM_{10}. Aerosol types such as sulfate, methanesulfonate, nitrate, ammonium, black carbon, primary organic carbon, sodium, calcium, chloride, carbonate, aerosol liquid water, and other inorganic matter (e.g., trace metals and silica) are involved in the simulation.
245   Dust was simulated with the GOCART dust emission scheme (Ginoux et al., 2001). The dust particulates were aggregated into the other inorganic matter component and were presented in the calculation of aerosol optical properties with anthropogenic aerosols.

Aerosol optical properties were calculated as a function of wavelength based on the Mie theory. The aerosol components within each size bin are assumed to be internally mixed. The mixing refractive indexes are the volume-weight average in
250   refractive indexes of all aerosol components. Aerosol extinction and scattering coefficients and asymmetric factors for a particulate per size bin are attained though searching a look-up Mie table by Chebyshev polynomial interpolation with the desired mixing refractive indexes and wet particulate radius. The value of particulate extinction coefficient multiplied with the particulate number concentration is volume extinction coefficient which is then multiplied with the height of layer to attain the layer *AOD* value. The sum of all layer *AOD* values over the four size bins is the columnar total *AOD* and is used for calculating
255   *AOD* increments in the assimilation.

3.3.2 Assimilation system

Gridpoint Statistical Interpolation (GSI) 3DVAR assimilation system (Wu et al., 2002; Kleist et al., 2009) version 3.7 was applied to improve the simulated aerosols by assimilating the aerosol measurements at Kashi. This GSI version has been modified to assimilate the aerosol products (Liu et al., 2011; Schwartz et al., 2012). We assimilated our ground-based multi-
260   wavelength *AOD* (440, 675, 870, 1020 nm) and the surface-layer concentrations of $PM_{2.5}$ and PM_{10} suited to the MOSAIC aerosol module in WRF-Chem. We used the natural logarithm of particulate number concentration per size bin as control variables. The aerosol dry mass concentrations, particulate number concentrations and aerosol water contents are converted

into *AOD* per size bin using the WRF-Chem aerosol optical routine. The adjoint observation operators for *AOD* and particulate matter are given as

$$\frac{\delta \ln(\tau)}{\delta \ln(n_i)} = \frac{n_i}{\tau} \cdot \frac{\delta \tau}{\delta n_i} = \frac{c_i}{\tau} \cdot e_i = \frac{\tau_i}{\tau}, \tag{7}$$

$$\frac{\delta \ln(c)}{\delta \ln(n_i)} = \frac{n_i}{c} \cdot \frac{\delta c}{\delta n_i} = \frac{n_i}{c} \cdot r_i, \tag{8}$$

where n_i is aerosol number concentration in the *i*th size bin, τ and c are the observed *AOD* and particulate matter mass concentrations. As no aerosol extinction coefficient assimilated in this experiment, we assume the extinction coefficient per size bin is constant in grid at each model layer. Innovation of number concentration due to *AOD* constraint is therefore a proportion of change in model layer *AOD* to the observed columnar *AOD*, which is attained via iteration to minimize the cost function. Innovation of number concentration due to the constraints of $PM_{2.5}$ and PM_{10} are associated with the ratios (r_i) of mass concentrations to number concentrations in a size bin estimated in the guess field, weighted by the proportion of the size number concentration, changing in the iteration, to the total particulate matter concentration.

3.3.3 Experimental setup

Initial and lateral boundary conditions for the meteorological fields in the WRF-Chem simulations were generated from the National Centers for Environmental Prediction (NCEP) Final Analysis (FNL) data using the Global Forecast System (GFS) model at a horizontal resolution of 1°. The boundary conditions were updated every 6 h and then interpolated linearly in time by WRF-Chem. Anthropogenic emissions from the 2010 MIX emission inventories (www.meicmodel.org) containing the Multiresolution Emission Inventory of China (MEIC) were used in the simulations. The biogenic emissions were estimated using the Model of Emissions of Gases and Aerosols from Nature (MEGAN; Guenther et al., 2006). Two one-month WRF-Chem simulations were performed for April 2019, discarding a one-week spin-up at the beginning of each simulation. The first one-month simulation was used for modelling background error covariance (BEC). The second one-month simulation was assimilated the observations of $PM_{2.5}$, PM_{10} and *AOD* with GSI at 0:00, 6:00, 12:00 and 18:00 UTC with the assimilation window of ±3 h centered at the analysis times. The model was restarted from the meteorology and chemistry at analysis time and ran to the next analysis time. For the second one, each restart called the radiation routines twice which included and excluded the aerosols, respectively, and the corresponding difference between the two calls in irradiances is aerosol radiative forcing.

A general way to model BEC is the National Meteorological Center (NMC) method that computes the statistical differences between two forecasts with different leading lengths (e.g. 12 and 24 h, or 24 and 48 h) but valid at the same time (Parrish and Derber, 1992). However, in our experiment, the WRF-Chem model strongly underestimated aerosol concentrations and hence likely lowered the error magnitudes. For this reason, we assessed the standard deviations of the control variables over the entire one-month period at the four analysis hours (00, 06, 12, 18 h), respectively. Each standard

deviation field was used for modelling a BEC repeatedly applied in the assimilations at the corresponding analysis hour. This approach represents the strong fluctuations of control variables as weather evolution during clear and dusty days. We expect
295 fluctuations of aerosols over the different weathers are larger than the uncertainties due to different leading forecast lengths and may give a better input field for modelling BEC. The observation errors for *AOD* and *PM* were 50% of natural logarithm of 0.01 and those errors of *PM* including measurement error and representative error depending on the grid size and the *PM* concentrations (Schwartz et al., 2012). The choice of 50% was determined by trying experimentally with different values, which can effectively assimilate measurements and will not excessively damage the model results.

4 Results and Discussion

4.1 Aerosol solar radiative forcing and efficiency

Results of instantaneous *ASRF* and *ASRFE* at TOA, in ATM, at BOA during the DAO-K campaign are given in Fig. 5. Both positive and negative values of *ASRF*, corresponding to warming and cooling effects respectively, can be found at top of the atmosphere (Fig. 5a). However, aerosols have only warming effects in the atmosphere (Fig. 5c) and cooling effects at the
305 surface (Fig. 5e) during the DAO-K campaign. *ASRF*s at the TOA and BOA exhibit obvious negative correlations with *AOD*. But positive correlation can be observed between *ASRF* in the atmosphere and *AOD*. From Fig. 5, it is evident that the dust aerosol has strong influences on the solar radiation budget. For the five aforementioned high aerosol loading episodes (see Sect. 2.2), the dust-dominant aerosols have stronger cooling effects at the TOA and BOA, and more significant warming effects in the atmosphere than other low aerosol loading situations. Moreover, the cooling effects at the BOA are more noticeable than
310 which at the TOA, with the lowest values of -217 W m^{-2} and -119 W m^{-2}, respectively.

When *ASRF* is normalized by aerosol optical depth at 550 nm, the result of *ASRFE* is not sensitive to the aerosol loading. However, a weak negative correlation between *ASRFE* and *AE* can also be observed at the BOA (Fig. 5f). That means, the *ASRFE* at the surface can roughly indicate the radiative forcing effects of different types of aerosols (García et al., 2008). Relatively large fraction of small particles associated with large *AE* has stronger *ASRFE* for cooling the surface than other low
315 *AE* situations. But for TOA and ATM, there are no obvious correlations between *ASRFE* and *AE*. Globally the cooling effect of aerosols at Kashi is more efficient at the BOA than that at the TOA. That is in accordance with the results of *ASRF*. In comparison with *ASRF*, the variation of *ASRFE* is relatively moderate during the campaign. The strongest cooling effects on the TOA and BOA all appear in the episode of dust storm outbreak (i.e., 24 and 25 April 2019). But large dust particles in this case do not show extreme radiative forcing efficiency. Strong cooling efficiencies at the surface during the DAO-K campaign
320 occur in the very clear cases with high *AE* on 7 April 2019 (Fig. 5f).

During the DAO-K campaign, the average values of daily mean *ASRF* at Kashi are -19±13 W m^{-2} at the TOA and -36±23 W m^{-2} at the BOA, which are slightly stronger than the multiyear average values at this site (i.e., -16 W m^{-2} at the TOA and -18 W m^{-2} at the BOA) obtained by the previous study (Li et al., 2018). These results are reasonable, since the campaign was performed in the dust-prone season and higher aerosol loading situations have stronger *ASRF* effects as discussed above.

325   Likewise, the average values of daily mean *ASRFE* at the TOA and BOA during the DAO-K campaign are -27±9 W m^{-2} τ_{550}^{-1} and -55±10 W m^{-2} τ_{550}^{-1}, respectively, which are more efficient than the corresponding multiyear average values (i.e., -21 W m^{-2} τ_{550}^{-1} at the TOA and -24 W m^{-2} τ_{550}^{-1} at the BOA) reported in the previous study (Li et al., 2018).
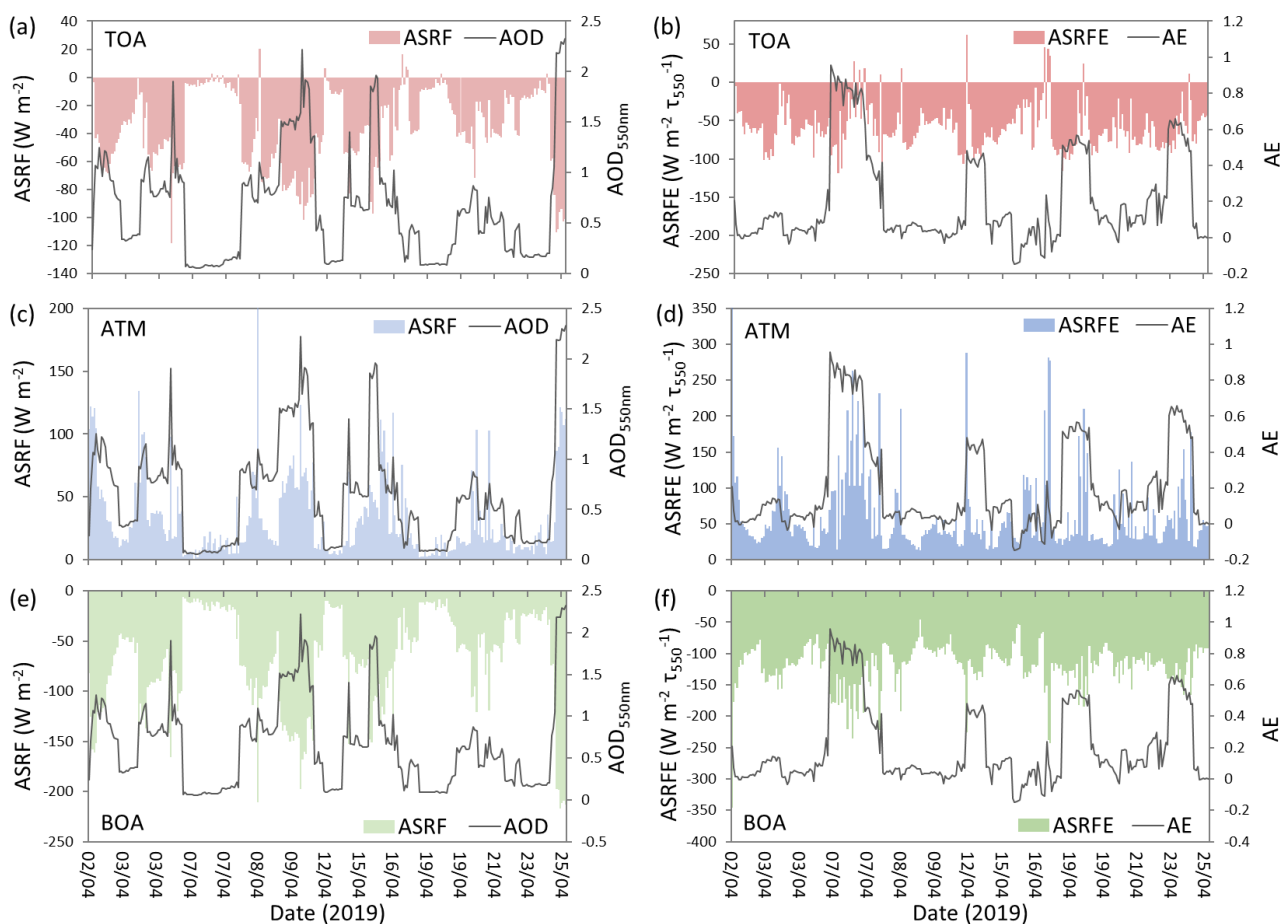
330   **Figure 5: Instantaneous aerosol solar radiative forcing (left column) and efficiencies (right column) at Kashi site during the DAO-K campaign (upper panels: TOA; middle panels: ATM; lower panels: BOA).**

4.1.1 Clear sky case

Instantaneous *ASRF* and *ASRFE* of the clear sky case on 7 April 2019 is depicted in Fig. 6. It was a typical cloud-free day at Kashi with *AOD* at 550 nm less than 0.22 for the whole day. As discussed above, the highest *AE* is observed on this day during

335   the one-month campaign (see Fig. 3). Both cooling and warming effects of aerosols can be found at the top of atmosphere. The cooling effects of *ASRF* are up to -19 W m^{-2} at the TOA and -48 W m^{-2} at the BOA, and the warming effect of *ASRF* is up to 50 W m^{-2} in the atmosphere. The corresponding extreme *ASRFE* values are -126, -236, and 263 W m^{-2} τ_{550}^{-1}, respectively It is apparent that the changes of *ASRFE* are more intense than the corresponding *ASRF* for the clear case.
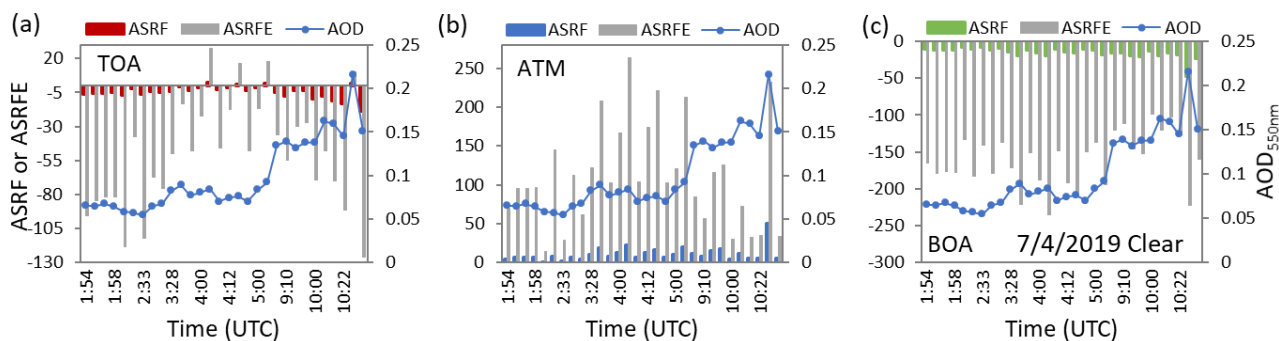
Figure 6: Instantaneous aerosol solar radiative forcing and efficiencies of the clear sky case on 7 April 2019 at Kashi site (a) TOA, (b) ATM, (c) BOA.

4.1.2 Heavy dust case

Fig. 7 describes *ASRF* and *ASRFE* for a heavy dust storm episode on 25 April 2019 at Kashi. Only few observations from 3:33 to 4:11 UTC were suitable for retrieval in this day. Aerosol optical depth at 550 nm was up to 2.3 during this observation period. In comparison with the clear case, dust particles have stronger cooling effects at the TOA and BOA (*ASRF*s up to -111 and -217 W m^{-2}, respectively), and stronger warming effect in ATM (*ASRF* up to 121 W m^{-2}). However, we observe the extreme *ASRFE* values of -51, -99, and 55 W m^{-2} τ_{550}^{-1} at the TOA, BOA, and in ATM, respectively, indicating that the radiative forcing of dust is less efficient than that of the clear case. Moreover, the variations of *ASRFE* in the dust case are more moderate than which of *ASRF*. These are strikingly different from the clear case.
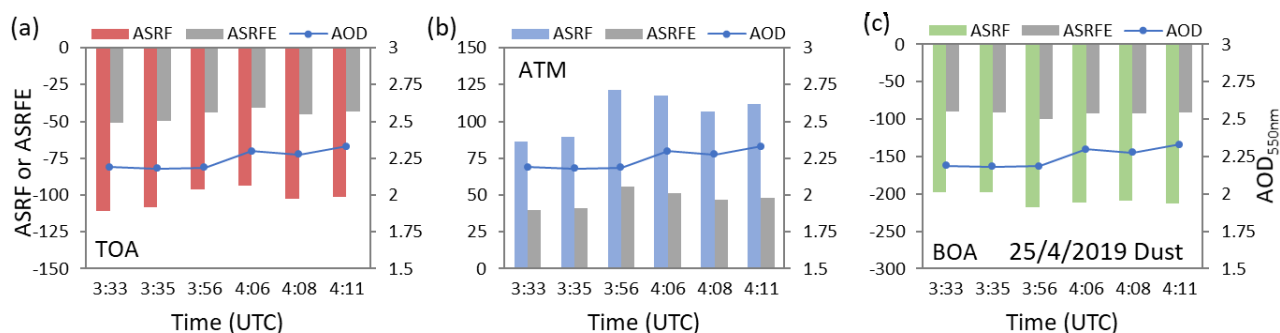
Figure 7: As Fig. 6, but for the heavy dust case on 25 April 2019.

4.1.3 Two-layer dust case

355

360

365

On 9 April 2019 one extra layer suspending above the planetary boundary layer (PBL) was observed. Fig. 8 illustrates the observations of LILAS on 8 April. Lidar observations on 9 April 2019 are not shown because the lidar stopped working due to technical problems in the night of 8 April 2019. According to the backscattering coefficient profiles at 355 nm, the lower layer and upper layer can be clearly identified. Lidar measurements indicate that aerosols in the layer above the PBL are probably dust particles because the derived high depolarization ratios agree with the values for dust. However, from lidar measurements we cannot draw unambiguous conclusion about the aerosol type in the PBL, because the incomplete overlap range of the lidar system is up to 800~1000 m. From Fig. 3, high AOD corresponding to low AE in the whole atmosphere and high $PM_{2.5}$ and PM_{10} concentrations in the surface layer are exhibited from 8 to 9 April. It also suggests the complex pollutions by two-layer dust particles during this pollution process. AOD at 550 nm on 9 April changes from 1.4 to 2.2 (Fig. 9). In consistent with the above heavy dust case, only cooling effects can be observed at the TOA and BOA, and only warming effect can be found in ATM for this case. The two layers of dust particles result in a TOA cooling up to -102 W m^{-2}, BOA cooling of up to -198 W m^{-2}, and atmosphere warming of up to 123 W m^{-2}. The absolute values of $ASRF$ in this case are all less than those in the heavy dust case, suggesting the aerosols in the heavy dust case have more powerful radiative forcing effects. Nevertheless, the extreme values of $ASRFE$ are -62, -105, and 58 W m^{-2} τ_{550}^{-1} at the TOA, BOA and in ATM, respectively, indicating that dust particles have similar radiative forcing efficiencies in the two-layer and heavy dust cases.
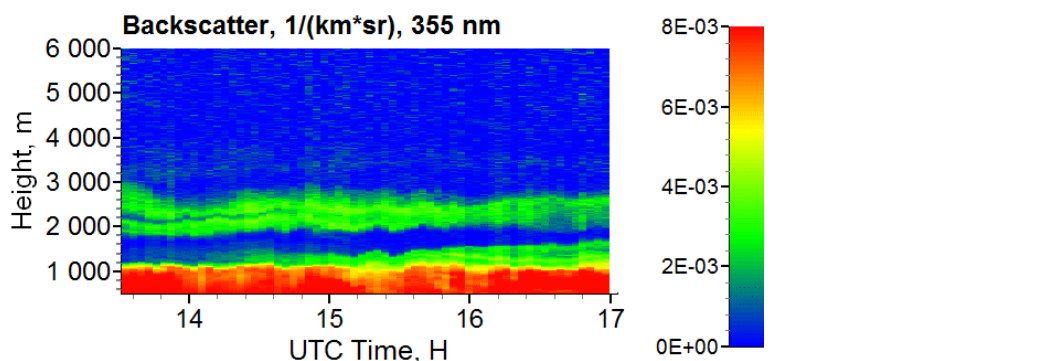
Figure 8: The backscattering coefficient profiles at 355 nm for the two-layer dust case in the night of 8 April 2019.
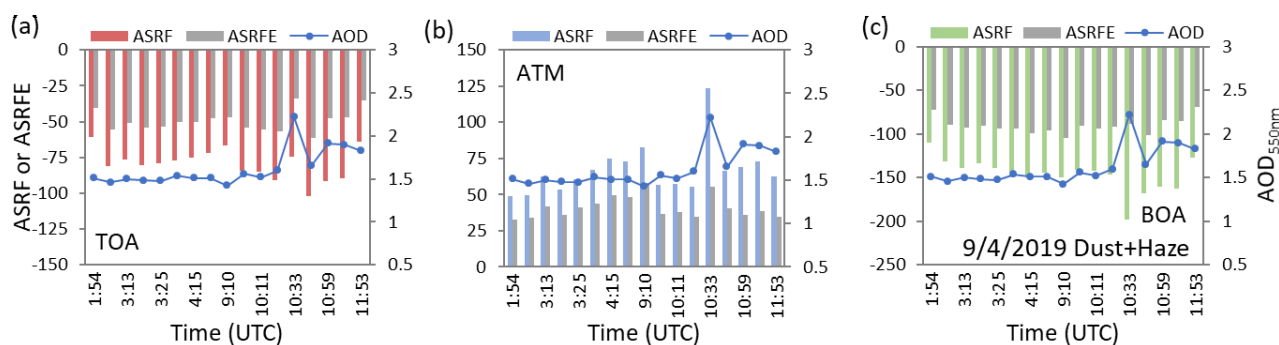
370   **Figure 9: As Fig. 6, but for the two-layer dust case on 9 April 2019.**

4.2 Influences of the atmosphere and surface conditions

Fig. 10 describes the influences of atmospheric profile and land surface albedo on the simulations of total irradiances and *ASRF*. The differences in the results of total downward irradiance (*TDI*), total upward irradiance (*TUI*), and *ASRF* at the TOA and BOA simulated with pre-defined midlatitude winter profile and user-specified profiles, and simulated with local noon
375 surface albedo and instantaneous surface albedo are given, respectively. According to Fig. 10a, different settings of profiles have no influence on the *TDI* at the TOA. For the *TUI*, the absolute differences are less than 9 W m^{-2}. However, the atmospheric profile has significant impacts on both the *TDI* and *TUI* at the surface. The influences on *TDI* are generally stronger than which on *TUI*. The maximum absolute difference is up to 138 W m^{-2} (Fig. 10c). For *ASRF* at the TOA, the effects of atmospheric profiles are less than 5 W m^{-2}. But the serious influences can up to 103 W m^{-2} on *ASRF* at the BOA (Fig. 10e). The average
380 effect of different profiles on *ASRF* is 0.8 W m^{-2} at the TOA, which is quite small in comparison with the average values of daily *ASRF* (-19 W m^{-2}). However, the average difference of 13 W m^{-2} for *ASRF* affected by atmospheric profiles cannot be ignored relative to the average *ASRF* (-36 W m^{-2}) at the BOA. As a result, the cooling effects of aerosol radiative forcing will be significantly underestimated at the BOA simulated with the pre-defined midlatitude winter profile instead of the user-specified Kashi profiles.

385   Like atmospheric profile, different settings of LSA have also no influence on *TDI* at the TOA (Fig. 10b). They have small effects on *TDI* at the BOA (absolute difference less than 3 W m^{-2}), but obvious impacts on *TUI* at the TOA and BOA (absolute difference up to 22 W m^{-2}) (Fig. 10 b,d). From Fig. 4, the local noon albedo is often less than the daily mean albedo. Especially for the clear day, the minimum of LSA occurs around the local noon. Then the *TUI* at the TOA and BOA will generally be underestimated by using the local noon albedo instead of instantaneous surface albedo in the simulations. But for *ASRF* (Fig.
390 10f), two LSA settings lead to moderate impacts at the TOA and BOA with average difference of 1.8 and 1.7 W m^{-2}, respectively. Therefore, simulations using the local noon albedo trend to overestimate the cooling effects of the aerosol radiative forcing both at the TOA and BOA.

395
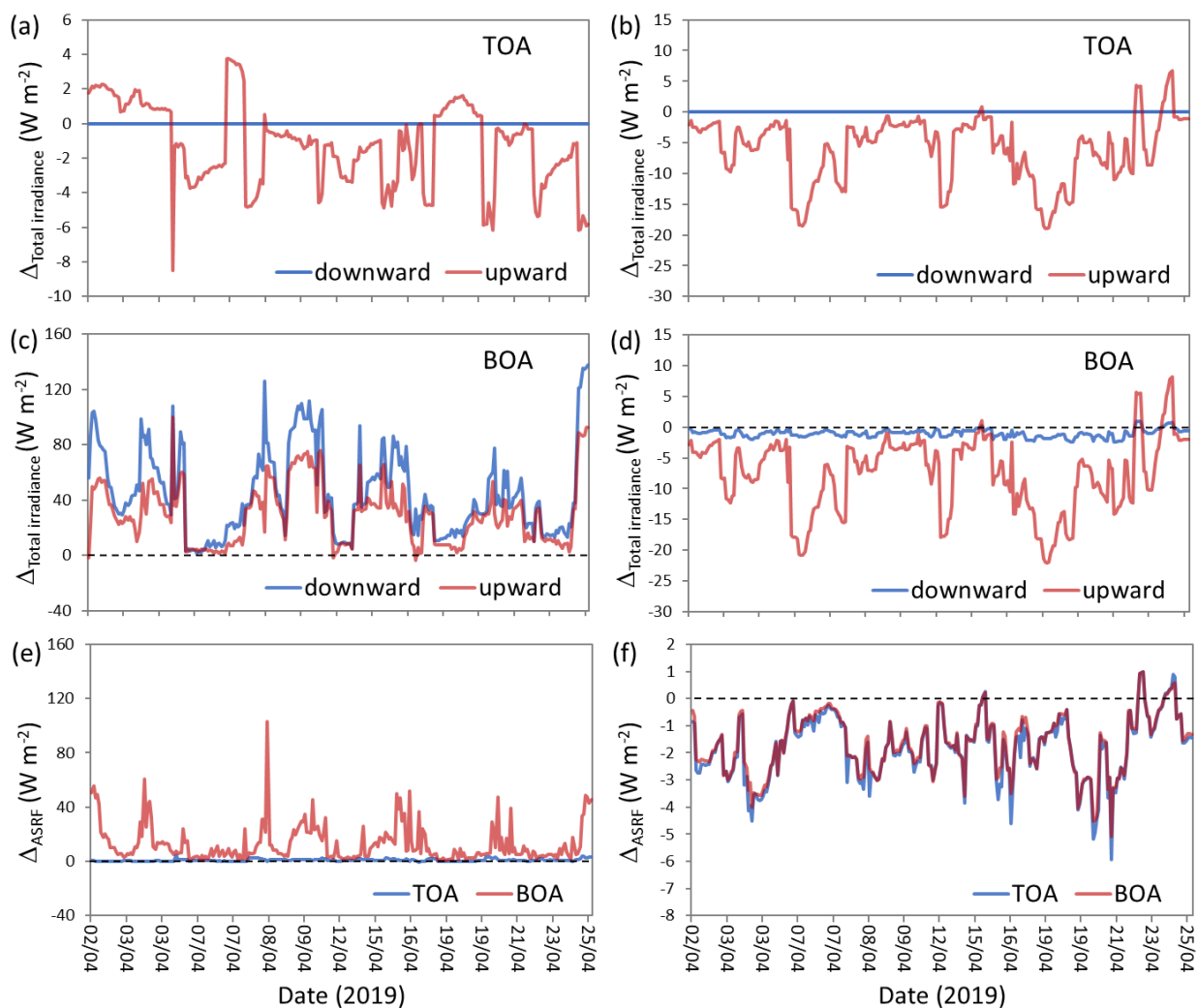
Figure 10: Influences of atmospheric profile (left column) and land surface albedo (right column) on total irradiances and *ASRF*. (a) difference of total downward and upward irradiances (*TDI* and *TUI*) at the TOA between simulations with pre-defined midlatitude winter profile and user-specified profiles; (b) difference of *TDI* and *TUI* at the TOA between simulations with local noon surface albedo and instantaneous surface albedo; (c) as (a), but for BOA; (d) as (b), but for BOA; (e) difference of *ASRF* between simulations
400 **with pre-defined midlatitude winter profile and user-specified profiles at the TOA and BOA; (f) difference of *ASRF* between simulations with local noon surface albedo and instantaneous surface albedo at the TOA and BOA.**

4.3 Comparisons and validation

In order to evaluate the results of aerosol radiative forcing comprehensively, we compare the radiative transfer simulations with the AERONET operational products and the WRF-Chem simulations. The downward irradiance at the surface directly
405 measured by high-precision solar radiation monitoring station during the DAO-K campaign are further adopted to validate the RT model and WRF-Chem model simulations.

4.3.1 Comparison between radiative transfer simulations and AERONET results

Aerosol radiative forcing at the TOA and BOA are operational products provided routinely by AERONET. Measurements of the CE318-T #1141 during the DAO-K campaign have been processed by AERONET. Therefore, we can compare the *ASRF*

410   product from AERONET with our simulations. It should be noted that AERONET adopts different definition of *ASRF* that only taking the downward irradiance at the BOA and the upward irradiance at the TOA into consideration. Omitting the downward irradiances with and without aerosols in the AERONET definition won't make much difference of *ASRF* at the TOA. But for *ASRF* at the BOA, neglecting the upward irradiance with and without aerosols in the AERONET definition will lead to obvious difference. Some existing studies have executed this kind of comparison (García et al., 2008; García et al.,

415   2012; Bi et al., 2014) and reported that AERONET trends to overestimate aerosol *ASRF* at the BOA (García et al., 2012).

Fig. 11 presents the correlations of instantaneous aerosol *ASRF* between the RT model simulations and the AERONET products. It is obvious that there are linear relationships between our RT simulations and the AERONET results with R^2 up to 0.98 and 0.99 at the TOA and BOA, respectively. Two *ASRF* results at the TOA show good consistency with a slope of 1.01, even though the calculated SW ranges are not an exact match (i.e., 0.28~3.0 μm for this study, and 0.2~4.0 μm for AERONET).

420   But for BOA, the AERONET products are obvious greater than the corresponding RT model simulations (with a slope of 1.24), which is in agreement with the conclusion of the previous study (García et al., 2012).
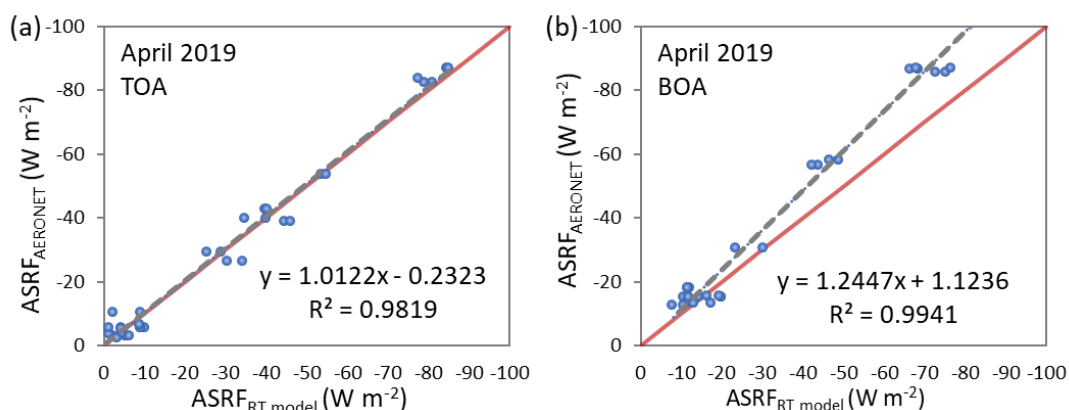
Figure 11: Correlations of instantaneous *ASRF* between radiative transfer (RT) model simulations and AERONET products at Kashi site during the DAO-K campaign (a) TOA, (b) BOA.

425   ### 4.3.2 Comparison between radiative transfer model and WRF-Chem model simulations

Fig. 12 compares the assimilated aerosols to the observations. Evidently, the assimilation greatly improves the particulate matter concentrations and show reasonable variations in accordance with the dust episodes. However, two disadvantages are noticeable. One is the assimilation fails to reproduce the extremely high $PM_{2.5}$ and PM_{10} on 24~25 April 2019, because the BEC is not specific for the model error in the strong dust storm. A better model result for the specific dust storm requires

430   improving the model capability of simulating dust emission and the transport of dust particulates besides data assimilation. Another is the assimilated *AOD* indeed increases but not well approaches the observations. The reason is that we only

assimilated *AOD* by assuming the invariable extinction coefficients. Hence, this low bias in *AOD* cannot be eliminated by choosing a scaling factor smaller than 50% in the observation error for it will damage the surface-layer particulate results. As a result, we give a priority to the high quality of the surface-layer aerosol assimilation, and the aerosol optical depth in the
435   assimilated WRF-Chem results is underestimated, which should be kept in mind when comparing the WRF-Chem results with the RT model simulations.
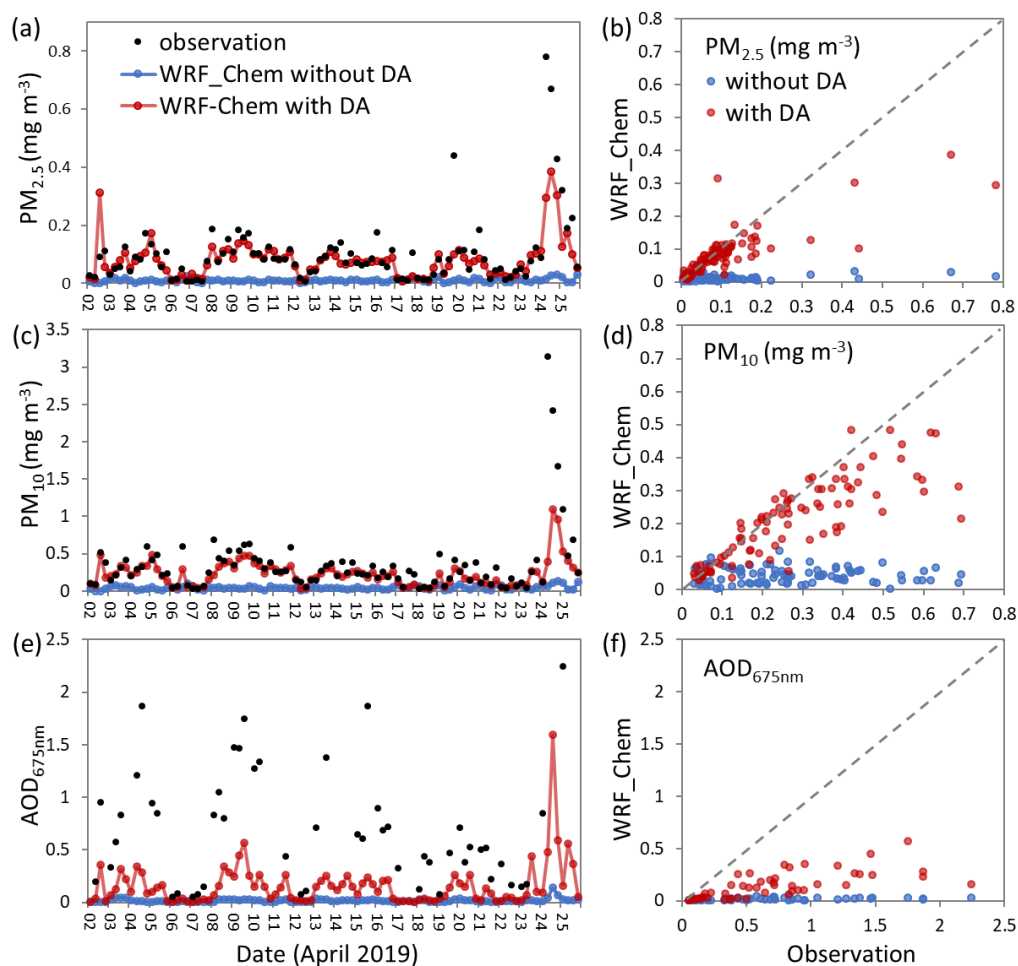
Figure 12: Comparisons of the surface-layer *PM2.5* (a, b), *PM10* (c, d) concentrations and *AOD* at 675 nm (e, f) among the observations, the WRF-Chem simulations with and without data assimilations (DA) in April 2019.

440   Fig. 13 illustrates the results of daily mean *ASRF*s during DAO-K campaign simulated by the SBDART radiative transfer and WRF-Chem models. Two results show similar variation patterns. However, it is notable that the WRF-Chem results are significantly greater than which of RT simulations in dust-polluted cases on 9, 24, and 25 April 2019. According to RT simulations, the strongest radiative forcing occurred on 25 April 2019. However, the most significant *ASRF* of WRF-Chem simulation is found on 24 April 2019 followed by 25 April 2019. As mentioned above, heavy dust storms broke out on these
445   two days during the DAO-K campaign. The extreme values of daily mean *ASRF* calculated by RT model are -46 W m^{-2} at the

TOA, 48 W m^{-2} in ATM, and -94 W m^{-2} at the BOA, but with respect to the WRF-Chem simulations, the corresponding values are -78, 101, and -178 W m^{-2}, respectively. The significant differences between the two kinds of simulated results in dust cases should be further evaluated.
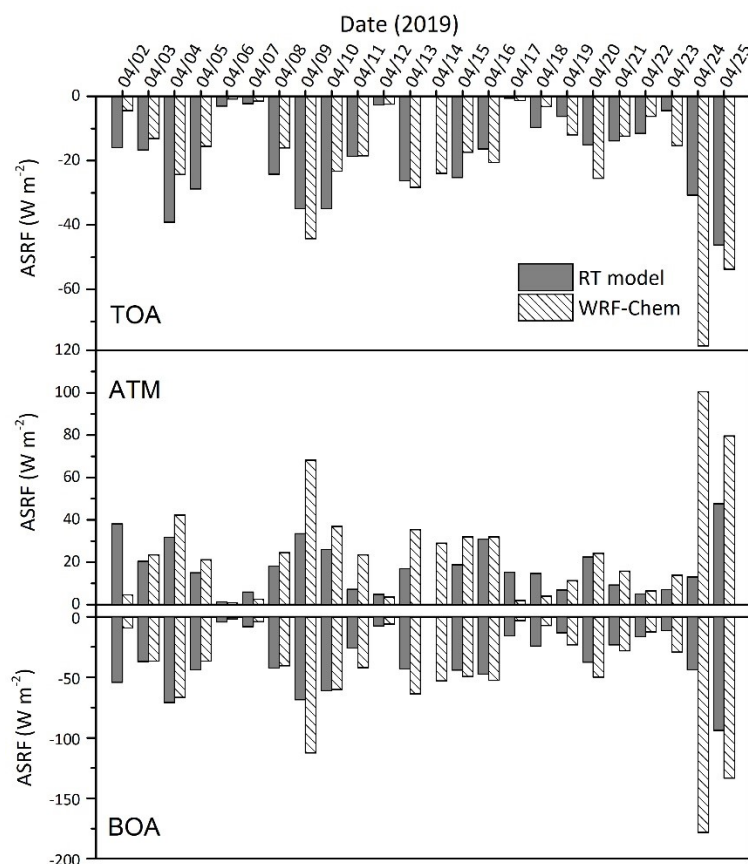
Figure 13: Comparisons of daily mean *ASRF* between the RT model calculations and the WRF-Chem simulations at Kashi site during the DAO-K campaign (upper panel: TOA; middle panel: ATM; lower panel: BOA).

4.3.3 Validation by ground-based irradiance measurements

Fig. 14 directly compares the RT and WRF-Chem simulated downward irradiances at surface with the ground-based measurements under three different sky conditions (i.e., clear case, heavy dust case, and two-layer dust case). The RT simulations of total, direct, and diffuse downward irradiances in the three situations agree well with high-precision measurements of pyrheliometer and pyranometers. The percent differences of RT-simulated total irradiance with respect to the measurements are only 0.03% for the clear case, -2.67% for the heavy dust case, and -0.43% for the two-layer dust case. Except for the heavy dust case, they are within the pyranometer measurement uncertainties (0.66%). As for the WRF-Chem simulations, the total irradiances in the clear sky case are consistent with RT simulations and measurements (Fig. 14a). But for the direct irradiances, there are obvious differences between the WRF-Chem simulations and the corresponding measurements

(Fig. 14b). Moreover, the WRF-Chem simulated diffuse irradiances in the clear case (Fig. 14c), the total, direct, and diffuse irradiances in the heavy dust and two-layer dust cases (Fig. 14d~i) are significantly distinct from the measurements and RT simulations.

465 One of the most noticeable features in the curves of WRF-Chem results is the sudden jump around 6:00 UTC, which can be attributed to data assimilations restarted at 6:00 UTC and ran to the next analysis time 12:00 UTC. The WRF-Chem results are greatly improved after 6:00 UTC in the dust-polluted cases. It is evident that data assimilations at 6:00 UTC can ameliorate the WRF-Chem simulations in dust cases, but the correction effects are still limited. So, the problems of the WRF-Chem simulation have not yet been fully resolved by the assimilations of aerosol optical depth and particulate matter concentrations. This conclusion is in accordance with Figs. 12 and 13. Our measurements have proved that the simulations of RT model are

470 reliable in both of clear and high aerosol loading situations. The WRF-Chem model preforms better in clear sky than in the dust-polluted conditions. There is still room for improving the WRF-Chem simulation of dust aerosol radiative forcing.
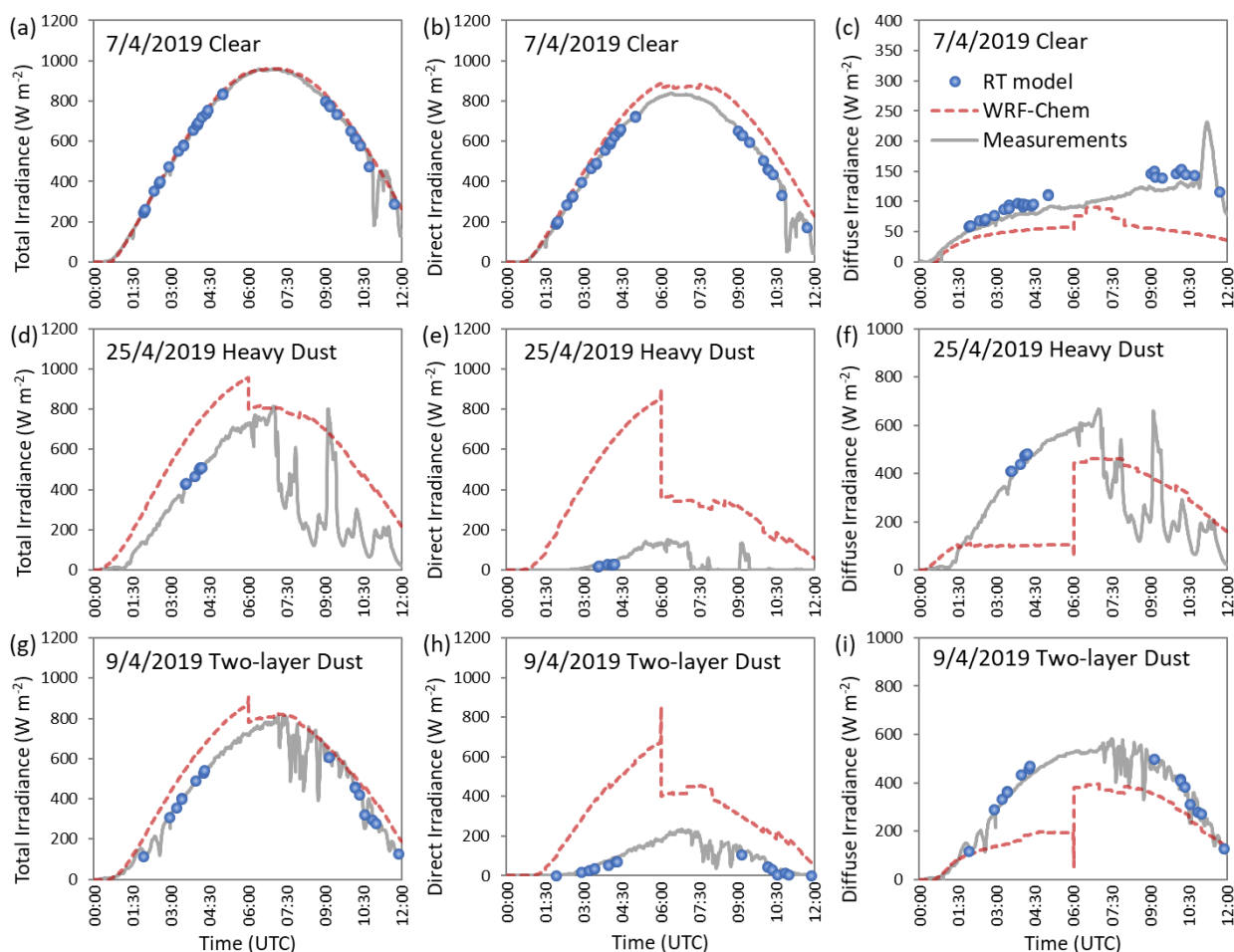
Figure 14: Comparisons of total, direct and diffuse downward irradiances at the bottom of atmosphere for the clear case (upper three panels), the heavy dust case (middle three panels), and the two-layer dust case (lower three panels) at Kashi site (blue points:

475   **simulated by the RT model; red dash lines: simulated by the WRF-Chem model with data assimilations at 0:00 and 6:00 UTC; gray solid lines: measured by pyrheliometer and pyranometers).**

5 Summary and conclusions

Dust aerosol particles play an important role in local and global climate changes by influencing the radiation budget through scattering and absorbing processes, especially for the region close to dust sources such as deserts. The complicated scattering
480 and absorption characteristics of dust particles make it challenging to estimate their direct radiative forcing. Therefore, the Dust Aerosol Observation-Kashi (DAO-K) campaign was designed and preformed near the Taklimakan desert that is a substantial and stable source of Asian dust aerosol particles. For almost one month, comprehensive observations of aerosol properties (i.e., aerosol optical depth, Ångström exponent, single scattering albedo, and asymmetry factor), atmospheric profiles (including ozone profiles), and land surface properties were obtained by a variety of ground-based and satellite
485 apparatus in the dust borne season, and were applied in aerosol solar radiative forcing analysis using the SBDART radiative transfer model simulations. In addition to high-quality dataset of volume aerosol properties satisfying the AERONET and SONET level 1.5 data criteria, the daily specified atmospheric profiles and diurnal variations of land surface albedo were also considered in detail in the simulations. The simulated results show that the average values of daily mean *ASRF* at Kashi are -19 W m^{-2} at the TOA and -36 W m^{-2} at the BOA during the DAO-K campaign. The dust-dominant aerosols have stronger
490 cooling effects at both the top and bottom of atmosphere, and more significant warming effects in the atmosphere than other low aerosol loading situations. Nevertheless, the radiative forcing efficiencies in dust-polluted cases exhibit lower than those in clear-sky conditions. The average influences of different profiles on *ASRF* are small at the TOA (0.8 W m^{-2}) but remarkable at the BOA (13 W m^{-2}). The cooling effects of aerosol radiative forcing at the BOA will be significantly underestimated by simulations with the pre-defined midlatitude winter profile instead of the user-specified Kashi profiles. Simulations using the
495 local noon albedo trend to overestimate the cooling effects of the aerosol radiative forcing both at the TOA and BOA. Different land surface albedo settings lead to moderate impacts on *ASRF* with average effects of 1.8 W m^{-2} at the TOA and 1.7 W m^{-2} at the BOA.

    By assimilating the multi-wavelength volume *AOD* and the surface-layer *PM*$_{2.5}$ and *PM*$_{10}$ mass concentrations, the aerosol solar radiative forcing was also simulated for the time period of DAO-K field campaign using the WRF-Chem model. The
500 measurements of downward irradiances at the surface were applied in evaluating the two kinds of simulations. By comparison of the daily mean *ASRF*, two results present similar variation patterns. However, the WRF-Chem results are significantly stronger than the RT simulations in dust-polluted cases. For the heavy dust episode, the percent difference of daily mean *ASRF* between RT model and WRF-Chem model simulations are greater than 50% at the TOA, BOA, and in ATM. The direct, diffuse (and the sum of both) downward irradiances simulated by RT model in the clear sky, heavy dust, two-layer dust
505 conditions are all in good agreement with ground-based measurements. As for the WRF-Chem simulations, the total irradiances in the clear sky case are consistent with RT calculations and measurements. But the direct, diffuse, and total irradiances simulated by WRF-Chem significantly deviate from measurements in the dust-polluted situations. Data assimilations can

obvious improve the WRF-Chem simulations in dust cases, but the correction effects are still limited. Based on these findings it is concluded that the SBDART radiative transfer model provides credible estimates of dust particle solar radiative forcing if
510   supplied with reliable model inputs, but the WRF-Chem model is prone to overestimate the radiative forcing effects of dust aerosols. Considering the actual measured atmospheric profiles and diurnal variations of land surface albedo can improve the radiative transfer model simulations. Optimizations of dust emission scheme, background error setting of dust assimilation system, dust parameterization including nonsphericity, are proposed as the promising approaches to improve the WRF-Chem simulations of dust radiative forcing. We would like to emphasize, however, that the comparison is only conducted at one site
515   and in a limited time period in this study. Future research on this topic should include a systematic evaluation of RT and WRF-Chem model simulations on larger space and time scales.

Data availability. The MODIS, OMI, and AERONET products can be accessed at https://modis.gsfc.nasa.gov/, https://disc.gsfc.nasa.gov/, and https://aeronet.gsfc.nasa.gov/, respectively (last accessed July 2019).
520

Competing interests. The authors declare that they have no conflict of interest.

Acknowledgements. This research was funded by the National Natural Science Foundation of China (NSFC), grant number 41871271, and the National Key R&D Program of China, grant number 2016YFE0201400. The authors acknowledge the
525   groups of MODIS, OMI, and AERONET for making the surface albedo, ozone profile, and radiative forcing products available, respectively. We also thank the Kashi regional meteorological bureau and the China National environmental monitoring centre for providing the data of atmospheric sounding and PM_{10} concentration of Kashi, respectively. The Anhui Yunnengtian Intelligent Technology Co., Ltd., China is acknowledged for providing the Cloud Cover Automatic Observation Instrument and technical support. The first author also wishes to thank Haofei Wang, Thierry Podvin, Igor Veselovskiy, Jie Chen, and
530   Ying Zhang for participating the measurements.

References

Adesina, A. J., Kumar, K. R., Sivakumar, V., and Griffith, D.: Direct radiative forcing of urban aerosols over Pretoria (25.75°S, 28.28°E) using AERONET Sunphotometer data: first scientific results and environmental impact, Journal of Environmental Sciences-china, 26, 2459-2474, doi: 10.1016/j.jes.2014.04.006, 2014.

535   Ansmann, A., Petzold, A., Kandler, K., Tegen, I., Wendisch, M., Müller, D., Weinzierl, B., Müller, T., and Heintzenberg, J.: Saharan Mineral Dust Experiments SAMUM-1 and SAMUM-2: What have we learned? Tellus, 63B, 403-429. doi:10.1111/j.1600-0889.2011.00555.x, 2011.

Babu, S. S., Satheesh, S. K., and Moorthy, K. K.: Aerosol radiative forcing due to enhanced black carbon at an urban site in India, Geophys. Res. Lett., 29, 27-21, doi:10.1029/2002GL015826, 2002.

540 Bhartia, P. K., Mcpeters, R. D., Mateer, C. L., Flynn, L. E., and Wellemeyer, C. G.: Algorithm for the estimation of vertical ozone profiles from the backscattered ultraviolet technique, J. Geophys. Res., 101, 18793-18806, doi: 10.1029/96JD01165, 1996.

Bi, J., Huang, J., Hu, Z., Holben, B. N., and Guo, Z.: Investigating the aerosol optical and radiative characteristics of heavy haze episodes in Beijing during January of 2013, J. Geophys. Res. Atmos., 119, 9884-9900, doi: 10.1002/2014JD021757, 545 2014.

Bierwirth, E., Wendisch, M., Ehrlich, A., Heese, B., Tesche, M., Althausen, D., Schladitz, A., Müller, D., Otto, S., Trautmann, T., Dinter, T., von Hoyningen-Huene, W., and Kahn, R.: Spectral surface albedo over Morocco and its impact on radiative forcing of Saharan dust, Tellus, 61B, 252-269, DOI: 10.1111/j.1600-0889.2008.00395.x, 2009.

Bory, A. J., Biscaye, P. E., and Grousset, F. E.: Two distinct seasonal Asian source regions for mineral dust deposited in 550 Greenland (NorthGRIP), Geophys. Res. Lett., 30, 1167, doi:10.1029/2002GL016446, 2003.

Chen, S., Huang, J., Zhao, C., Qian, Y., Leung, L. R., and Yang, B.: Modeling the transport and radiative forcing of Taklimakan dust over the Tibetan Plateau: A case study in the summer of 2006, J. Geophys. Res. Atmos., 118, 797-812, doi:10.1002/jgrd.50122, 2013.

Chen, S., Zhao, C., Qian, Y., Leung, L. R., Huang, J., Huang, Z., Bi, J., Zhang, Y., Shi, J., Yang, L., Li, D., and Li, J.: Regional 555 modeling of dust mass balance and radiative forcing over East Asia using WRF-Chem, Aeolian Research, 15, 15-30, http://dx.doi.org/10.1016/j.aeolia.2014.02.001, 2014.

Chen, S., Yuan, T., Zhang, X., Zhang, G., Feng, T., Zhao, D., Zang, Z., Liao, S., Ma, X., Jiang, N., Zhang, J., Yang, F., and Lu, H.: Dust modeling over East Asia during the summer of 2010 using the WRF-Chem model, J. Quant. Spectrosc. Radiat. Transfer, 213, 1-12, https://doi.org/10.1016/j.jqsrt.2018.04.013, 2018.

560 Dubovik, O., Sinyuk, A., Lapyonok, T., Holben, B. N., Mishchenko, M., Yang, P., Eck, T. F., Volten, H., Munõz, O., Veihelmann, B., van der Zande, W. J., Leon, J. F., Sorokin, M., and Slutsker, I.: Application of spheroid models to account for aerosol particle nonsphericity in remote sensing of desert dust, J. Geophys. Res., 111, doi:10.1029/2005JD006619, 2006.

Esteve, A. R., Estelles, V., Utrillas, M. P., and Martinezlozano, J. A.: Analysis of the aerosol radiative forcing over a 565 Mediterranean urban coastal site, Atmospheric Research, 137, 195-204, doi: 10.1016/j.atmosres.2013.10.009, 2014.

Fast, J. D., Gustafson Jr., W. I., Easter, R. C., Zaveri, R. A., Barnard, J. C., Chapman, E. G., Grell, G. A., and Peckham, S. E.: Evolution of ozone, particulates, and aerosol direct ra- diative forcing in the vicinity of Houston using a fully coupled meteorology–chemistry–aerosol model, J. Geophys. Res., 111, D21305, doi:10.1029/2005JD006721, 2006.

García, O. E., Díaz, A. M., Expósito, F. J., Díaz, J. P., Dubovik, O., Dubuisson, P., Roger, J. C., Eck, T. F., Sinyuk, A., 570 Derimian, Y., Dutton, E. G., Schafer, J. S., Holben, B. N., and García, C. A.: Validation of AERONET estimates of atmospheric solar fluxes and aerosol radiative forcing by ground-based broadband measurements, J. Geophys. Res. Atmos., 113, 6089-6098, doi:10.1029/2008JD010211, 2008.

García, O. E., Díaz, J. P., Expósito, F. J., Díaz, A. M., Dubovik, O., Derimian, Y., Dubuisson, P., and Roger, J. C.: Shortwave radiative forcing and efficiency of key aerosol types using AERONET data, Atmos. Chem. Phys., 12, 5129-5145, doi:10.5194/acp-12-5129-2012, 2012.

Ginoux, P., Chin, M., Tegen, I., Prospero, J. M., Holben, B., Dubovik, O., and Lin, S. J.: Sources and distributions of dust aerosols simulated with the GOCART model, J. Geophys. Res.,106, 20255-20273, 2001.

Grell, G. A., Peckham, S. E., Schmitz, R., McKeen, S. A., Frost, G., Skamarock, W. C., and Eder, B.: Fully coupled ''online'' chemistry within the WRF model, Atmos. Environ., 39, 6957– 6975, doi:10.1016/j.atmosenv.2005.04.027, 2005.

Guenther, A., Karl, T., Harley, P., Wiedinmyer, C., Palmer, P. I., and Geron, C.: Estimates of global terrestrial isoprene emissions using MEGAN (Model of Emissions of Gases and Aerosols from Nature), Atmos. Chem. Phys., 6, 3181-3210, 2006.

Holben, B. N., Eck, T. F., Slutsker, I., Tanré, D., Buis, J. P., Setzer, A., Vermote, E., Reagan, J. A., Kaufman, Y. J., Nakajima, T., Lavenu, F., Jankowiak, I., and Smirnov, A.: AERONET—A Federated Instrument Network and Data Archive for Aerosol Characterization, Remote Sens. Environ., 66, 1-16, 1998.

Hu, Q., Goloub, P., Veselovskii, I., Bravo-Aranda, J., Popovici, I. E., Podvin, T., Haeffelin, M., Lopatin, A., Dubovik, O., Pietras, C., Huang, X., Torres, B., and Chen, C.: Long-range-transported Canadian smoke plumes in the lower stratosphere over northern France, Atmos. Chem. Phys., 19, 1173–1193, https://doi.org/10.5194/acp-19-1173-2019, 2019.

Huang, J., Fu, Q., Su, J., Tang, Q., Minnis, P., Hu, Y., Yi, Y., and Zhao, Q.: Taklimakan dust aerosol radiative heating derived from CALIPSO observations using the Fu-Liou radiation model with CERES constraints, Atmos. Chem. Phys., 9, 4011-4021, doi:10.5194/acp-9-4011-2009, 2009.

Huang, J., Wang, T., Wang, W., Li, Z., and Yan, H.: Climate effects of dust aerosols over East Asian arid and semiarid regions, J. Geophys. Res. Atmos., 119, doi:10.1002/2014JD021796, 2014.

Intergovernmental Panel on Climate Change (IPCC): Climate change 2007: the physical science basis. Contribution of Working Group I to the Fourth Assessment Report of the Intergovernmental Panel on Climate Change, Cambridge University Press, Cambridge, United Kingdom and New York, USA, 2007.

Jäkel, E., Wendisch, M., and Mayer, B.: Influence of spatial heterogeneity of local surface albedo on the area-averaged surface albedo retrieved from airborne irradiance measurements, Atmos. Meas. Tech., 6, 527-537, doi:10.5194/amtd-6-527-2013, 2013.

Kaskaoutis, D. G., Kambezidis, H. D., Hatzianastassiou, N., Kosmopoulos, P. G., and Badarinath, K. V. S.: Aerosol climatology: dependence of the Angstrom exponent on wavelength over four AERONET sites. Atmos. Chem. Phys. Discuss., 7, 7347–7397, 2007.

Kleist, D. T., Parish, D. F., Derber, J. C., Treadon, R., Wu, W. S., and Lord, S.: Introduction of the GSI into the NCEP global data assimilation system, Weather Forecast, 24, 1691-1705, 2009.

Lenoble, J., Remer, L., and Tanré, D.: Aerosol Remote Sensing, Springer Berlin Heidelberg, doi:10.1007/978-3-642-17725-5, 2013.

Lewis, P. and Barnsley, M. J.: Influence of the sky radiance distribution on various formulations of the earth surface albedo, Proc. Conf. Phys. Meas. Sign. Remote Sen. Val d'Isere, France, 707–715, 1994.

Li, L., Li, Z., Li, K., Blarel, L., and Wendisch, M.: A method to calculate Stokes parameters and angle of polarization of skylight from polarized CIMEL sun/sky radiometers, J. Quant. Spectrosc. Radiat. Transfer, 149, 334-346, http://dx.doi.org/10.1016/j.jqsrt.2014.09.003, 2014.

Li, Z., Blarel, L., Podvin, T., Goloub, P., Buis, J.-P., and Morel, J.-P.: Transferring the calibration of direct solar irradiance to diffuse-sky radiance measurements for CIMEL Sun-sky radiometers, Appl. Opt., 47, 1368–1377, https://doi.org/10.1364/AO.47.001368, 2008.

Li, Z., Li, D., Li, K., Xu, H., Cheng, X., Chen, C., Xie, Y., Li, L., Li, L., Li, W., Lv, Y., Qie, L., Zhang, Y., and Gu, X.: Sun/sky radiometer observation netword with the extension of multi-wavelength polarization measurements, Journal of Remote Sensing, 19, 496-520, doi:10.11834/jrs.20144129, 2015.

Li, Z. Q., Xu, H., Li, K. T., Li, D. H., Xie, Y. S., Li, L., Zhang, Y., Gu, X. F., Zhao, W., Tian, Q. J., Deng, R. R., Su, X. L., Huang, B., Qiao, Y. L., Cui, W. Y., Hu, Y., Gong, C. L., Wang, Y. Q., Wang, X. F., Wang, J. P., Du, W. B., Pan, Z. Q., Li, Z. Z., and Bu, D.: Comprehensive Study of Optical, Physical, Chemical, and Radiative Properties of Total Columnar Atmospheric Aerosols over China: An Overview of Sun-Sky Radiometer Observation Network (SONET) Measurements, Bulletin of the American Meteorological Society, 99, 739-755, doi:10.1175/BAMS-D-17-0133.1, 2018.

Liang, S.: Quantitative Remote Sensing of Land Surfaces, John Wiley, Hoboken, 2004.

Liu, Z., Liu, Q., Lin, H. C., Schwartz, C. S., Lee, Y. H., and Wang, T.: Three-dimensional variational assimilation of MODIS aerosol optical depth: implementation and application to a dust storm over East Asia, J. Geophys. Res., 116, D23206, doi:10.1029/2011JD016159, 2011.

Lucht, W., Schaaf, C. B., and Strahler, A. H.: An algorithm for the retrieval of albedo from space using semiempirical BRDF models, IEEE Trans. Geosci. Remote Sens., 38, 977-998, 2000.

Mikami, M., Shi, G., Uno, I., Yabuki, S., Iwasaka, Y., Yasui, M., Aoki, T., Tanaka, T.Y., Kurosaki, Y., Masuda, K., Uchiyama, A., Matsuki, A., Sakai, T., Takemi, T., Nakawo, M., Seino, N., Ishizuka, M., Satake, S., Fujita, K., Hara, Y., Kai, K., Kanayama, S., Hayashi, M., Du, M., Kanai, Y., Yamada, Y., Zhang, X.Y., Shen, Z., Zhou, H., Abe, O., Nagai, T., Tsutsumi, Y., Chiba, M., and Suzuki, J.: Aeolian dust experiment on climate impact: An overview of Japan-China joint project ADEC, Global and Planetary Change, 52, 142-172, doi:10.1016/j.gloplacha.2006.03.001, 2006.

Minnis, P., Mayor, S., Smith, W. L., and Young, D. F.: Asymmetry in the diurnal variation of surface albedo, IEEE Trans. Geosci. Remote Sens., 35, 879–891, doi:10.1109/36.602530, 1997.

Otto, S., de Reus, M., Trautmann, T., Thomas, A., Wendisch, M., and Borrmann, S.: Atmospheric radiative effects of an in-situ measured Saharan dust plume and the role of large particles. Atmos. Chem. Phys., 7, 4887-4903, 2007.

Parrish, D. F. and Derber, J. C.: The National Meteorological Center's spectral statistical interpolation analysis system, Mon. Weather Rev., 120, 1747-1763, doi:10.1175/1520-0493(1992)120<1747:TNMCSS>2.0.CO;2, 1992.

640 Ricchiazzi, P., Yang, S., Gautier, C., and Sowle, D.: SBDART: A Research and Teaching Software Tool for Plane-Parallel Radiative Transfer in the Earth's Atmosphere, Bulletin of the American Meteorological Society, 79, 2101-2114, 1998.

Schaaf, C. B., Gao, F., Strahler, A. H., Lucht, W., Li, X., Tsang, T., Strugnell, N. C., Zhang, X., Jin, Y., Muller, J. P., Lewis, P., Barnsley, M., Hobson, P., Disney, M., Roberts, G., Dunderdale, M., Doll, C., d'Entremont, R. P., Hu, B., Liang, S., Privette, J. L., and Roy, D.: First operational BRDF, albedo nadir reflectance products from MODIS, Remote Sens.
645   Environ., 83, 135-148, 2002.

Schaaf, C. and Wang, Z.:MCD43A1 MODIS/Terra+Aqua BRDF/Albedo Model Parameters Daily L3 Global - 500m V006, NASA EOSDIS Land Processes DAAC, http://doi.org/10.5067/MODIS/MCD43A1.006, 2015.

Schwartz, C. S., Liu, Z., Lin, H. C., and McKeen, S. A.: Simultaneous three-dimensional variational assimilation of surface fine particulate matter and MODIS aerosol optical depth, J. Geophys. Res., 117, D13202, doi:10.1029/2011JD017383,
650   2012.

Stapf, J., Ehrlich, A., Jäkel, E., Lüpkes, C., and Wendisch, M.: Reassessment of the common concept to derive the surface cloud radiative forcing in the Arctic: Consideration of surface albedo-cloud interactions, Atmos. Chem. Phys. Discuss., https://doi.org/10.5194/acp-2019-534, in review, 2019.

Sun, H., Pan, Z., and Liu, X.: Numerical simulation of spatial-temporal distribution of dust aerosol and its direct radiative
655   effects on East Asian climate, J. Geophys. Res., 117, doi:10.1029/2011JD017219, 2012.

Tegen, I., Bierwirth, E., Heinold, B., Helmert, J., and Wendisch, M.: The effect of measured surface albedo on modeled Saharan dust radiative forcing, J. Geophys. Res., 115, D24312, doi:10.1029/2009JD013764, 2009.

Twomey, S.: The Influence of Pollution on the Shortwave Albedo of Clouds, J. Atmos. Sci., 34, 1149-1152, 1977.

Valenzuela, A., Olmo, F. J., Lyamani, H., Anton, M., Quirantes, A., and Alados-Arboledas, L.: Aerosol radiative forcing
660   during African desert dust events (2005–2010) over Southeastern Spain, Atmos. Chem. Phys., 12, 10331-10351, doi:10.5194/acp-12-10331-2012, 2012.

Veselovskii, I., Goloub, P., Podvin, T., Bovchaliuk, V., Derimian, Y., Augustin, P., Fourmentin, M., Tanre, D., Korenskiy, M., Whiteman, D. N., Diallo, A., Ndiaye, T., Kolgotin, A., and Dubovik, O.: Retrieval of optical and physical properties of African dust from multiwavelength Raman lidar measurements during the SHADOW campaign in Senegal, Atmos. Chem.
665   Phys., 16, 7013-7028, doi:10.5194/acp-16-7013-2016, 2016.

Veselovskii, I., Goloub, P., Podvin, T., Tanre, D., Silva, A. D., Colarco, P. R., Castellanos, P., Korenskiy, M., Hu, Q., Whiteman, D. N., Pérez-Ramírez, D., Augustin, P., Fourmentin, M., and Kolgotin, A.: Characterization of smoke and dust episode over West Africa: comparison of MERRA-2 modeling with multiwavelength Mie–Raman lidar observations, Atmos. Meas. Tech., 11, 949-969, https://doi.org/10.5194/amt-11-949-2018, 2018.

670 Wang, D., Liang, S., He, T., Yu, Y., Schaaf, C., and Wang, Z.: Estimating daily mean land surface albedo from MODIS data, J. Geophys. Res. Atmos., 120, 4825-4841, doi:10.1002/2015JD023178, 2015.

Wendisch, M., Hellmuth, O., Ansmann, A., Heintzenberg, J., Engelmann, R., Althausen, D., Eichler, H., Müller, D., Hu, M., Zhang, Y., and Mao, J.: Radiative and dynamic effects of absorbing aerosol particles over the Pearl River Delta, China, Atmos. Environ., 42, 6405-6416, doi:10.1016/j.atmosenv.2008.02.033, 2008.

675 Werner, F., Ditas, F., Siebert, H., Simmel, M., Wehner, B., Pilewskie, P., Schmeissner, T., Shaw, R. A., Hartmann, S., Wex, H., Roberts, G. C., and Wendisch, M.: Twomey effect observed from collocated microphysical and remote sensing measurements over shallow cumulus, J. Geophys. Res., 119, 1534-1545, doi:10.1002/2013JD020131, 2014.

Wu, W.S., Purser, R. J., and Parrish, D. F.: Three-dimensional variational analysis with spatially inhomogeneous covariances, Mon. Weather Rev., 130, 2905-2916, doi: 10.1175/1520-0493(2002)130<2905:TDVAWS>2.0.CO;2, 2002.

680 Zaveri, R. A., and Peters, L. K.: A new lumped structure photochemical mechanism for large-scale applications, J. Geophys. Res., 104, 30,387-30,415, doi: 10.1029/1999JD900876, 1999.

Zaveri, R. A., Easter, R. C., Fast, J. D., and Peters, L. K.: Model for Simulating Aerosol Interactions and Chemistry (MOSAIC), J. Geophys. Res., 113, D13204, doi:10.1029/2007JD008782, 2008.

Zhao, C., Liu, X., Leung, L. R., Johnson, B., Mcfarlane, S. A., Gustafson, W. I., Fast, J. D., and Easter, R. C.: The spatial
685 distribution of mineral dust and its shortwave radiative forcing over North Africa: modeling sensitivities to dust emissions and aerosol size treatments, Atmos. Chem. Phys., 10, 8821-8838, doi:10.5194/acp-10-8821-2010, 2010.